ACS Sustainable Chemistry & Engineering

pubs.acs.org/journal/ascecg

Research Article

Plasma Catalysis for Ammonia Synthesis: A Microkinetic Modeling Study on the Contributions of Eley−Rideal Reactions

Yannick Engelmann,* Kevin van 't Veer, Yury Gorbanev, Erik Cornelis Neyts, William F. Schneider, and Annemie Bogaerts

Cite This: *ACS Sustainable Chem. Eng.* 2021, 9, 13151−13163

Read Online

ACCESS | Metrics & More | Article Recommendations | Supporting Information

ABSTRACT: Plasma catalysis is an emerging new technology for the electrification and downscaling of NH_3 synthesis. Increasing attention is being paid to the optimization of plasma catalysis with respect to the plasma conditions, the catalyst material, and their mutual interaction. In this work we use microkinetic models to study how the total conversion process is impacted by the combination of different plasma conditions and transition metal catalysts. We study how plasma-generated radicals and vibrationally excited N_2 (present in a dielectric barrier discharge plasma) interact with the catalyst and impact the NH_3 turnover frequencies (TOFs). Both filamentary and uniform plasmas are studied, based on plasma chemistry models that provided plasma phase speciation and vibrational distribution functions. The Langmuir−Hinshelwood reaction rate coefficients (i.e., adsorption reactions and subsequent reactions among adsorbates) are determined using conventional scaling relations. An additional set of Eley−Rideal reactions (i.e., direct reactions of plasma radicals with adsorbates) was added and a sensitivity analysis on the assumed reaction rate coefficients was performed. We first show the impact of different vibrational distribution functions on the catalytic dissociation of N_2 and subsequent production of NH_3, and we gradually include more radical reactions, to illustrate the contribution of these species and their corresponding reaction pathways. Analysis over a large range of catalysts indicates that different transition metals (metals such as Rh, Ni, Pt, and Pd) optimize the NH_3TOFs depending on the population of the vibrational levels of N_2. At higher concentrations of plasma-generated radicals, the NH_3 TOFs become less dependent on the catalyst material, due to radical adsorptions on the more noble catalysts and Eley−Rideal reactions on the less noble catalysts.

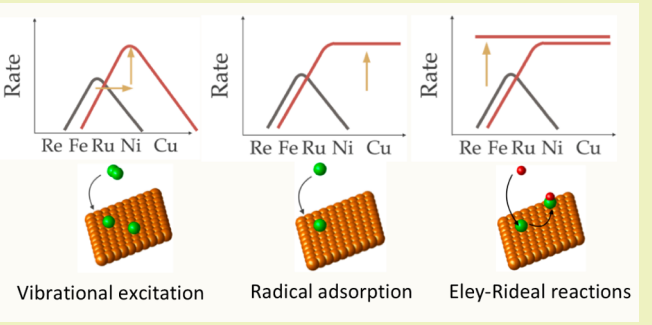

KEYWORDS: *Plasma catalysis, Eley−Rideal reactions, Volcano plots, Vibrational excitation, Radical reactions, Dielectric barrier discharge*

INTRODUCTION

For over a hundred years, the production of ammonia (NH_3) through the Haber−Bosch process has been one of the most important processes of chemical industry.[1] Efficient NH_3 synthesis from N_2 and H_2 is a crucial element in meeting today's agricultural needs, providing the building block for synthetic fertilizers. NH_3 can also be used as a hydrogen carrier and possibly holds the key to efficient hydrogen storage in a carbon-free economy.[2] Thermodynamically, NH_3 synthesis from N_2 and H_2 is an exergonic reaction at atmospheric pressure and ambient temperature, but rates over conventional metal catalysts are low due to the high activation barrier to dissociate N_2. For this reason, the Haber−Bosch process is carried out at elevated temperature (∼700 K) to increase the dissociation rate of N_2 and at elevated pressure (∼200 atm) to shift the equilibrium in favor of NH_3.

Vojdovic et al.[3] explored the requirements for a catalyst to promote NH_3 synthesis at ambient temperature and pressure along the conventional Langmuir−Hinshelwood (LH) pathway in which N_2 and H_2 dissociate at the catalyst surface and adsorbed N and H combine to form NH_3. They concluded that materials that follow the predicted linear relationships between activation and reaction energies on metal catalysts, will have negligible rates at these conditions. Mehta et al.[4] noted that these intrinsic material correlations would be shifted if applied to vibrationally excited N_2, as might be present in a nonthermal plasma. Model results predict that vibrational excitations would increase NH_3 synthesis rates at a given condition on materials kinetically limited by N_2 dissociation,[4,5] that the optimal catalytic material would be different from that at thermal conditions,[4] and that as consequence of nonthermal excitations,

Received: April 21, 2021
Published: September 21, 2021

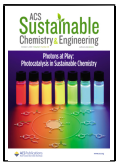

NH_3 yields could exceed equilibrium limits.[6] Results were supported by experimental observations over a variety of catalytic materials evaluated in a packed-bed dielectric barrier discharge (DBD) reactor, although direct comparisons of models and experiments are complicated by the confounding, reactive radical species generated within the DBD.

As reviewed by Mehta et al.,[5] the sensitivity of NH_3 productivity to catalyst choice in DBD plasma has been explored by a number of groups.[6−12] A consensus on an optimal material does not emerge from these observations, in part because experiments explore different plasma and reactor conditions as well as catalyst motifs. However, while observed turnover frequencies and yields vary with transition metals, the results are less sensitive to the catalyst material than would be suggested by the Mehta et al.[4] models. Furthermore, the DBD reactor produces some NH_3 even in the absence of a metal catalyst, and the reactor walls as well as the inner electrode are known to play a role in the NH_3 synthesis.[10,13]

Rouwenhorst et al.[14] defined NH_3 synthesis via an excitation-promoted LH pathway as *plasma-enhanced catalytic* synthesis. Other routes to NH_3 in a DBD plasma are defined as *surface-enhanced plasma-driven* synthesis or *plasma-enhanced semi-catalytic* synthesis.[14] In the former case, N_2 and H_2 are dissociated in the plasma phase and the surface aids in bringing the N and H radicals together to form NH_3. In the latter case, dissociation of N_2 occurs in the plasma phase and H_2 dissociation happens at the catalyst surface. Subsequent hydrogenation of N occurs at the catalyst surface. These two regimes couple plasma-generated radicals with the surface kinetics. In a given system, these other pathways could supplement or even supplant the thermal LH pathways.

The role of plasma-generated radicals can result in two different mechanisms, (i) a two-step mechanism where the radicals first adsorb to a free catalyst site and subsequently react with other adsorbates or (ii) a one-step mechanism where the radicals directly react with adsorbates (which are here collectively called Eley−Rideal, or ER reactions). Experimental works[15,16] have tried to pinpoint specific reaction routes via isotope tracing[15] and mass spectrometry and X-ray photoelectron spectroscopy.[16] These experiments show limited, indirect evidence for ER reactions without providing detailed mechanistic and kinetic information on the exact catalytic pathways.

Microkinetic models can provide the necessary information to elucidate the underlying mechanisms. Hong et al.[17] reported on a kinetic model for plasma-catalytic NH_3 synthesis in an atmospheric pressure discharge in contact with Al_2O_3 or Fe/Al_2O_3, with a reduced electric field (ratio of electric field over gas number density, typically expressed in Td, where 1 Td = 10^{-21} V m^2) in the range of 30−50 Td. The surface reactions included both LH and ER reactions and the reaction rates were determined based on (often estimated) sticking coefficients. The calculation results suggested that the main catalytic pathway for NH_3 synthesis is a combination of plasma phase dissociation and recombination, followed by both LH and ER reactions on the catalyst. First, N_2 dissociates in the plasma phase, (i) $e^- + N_2 \rightarrow e^- + 2N$, and then the subsequent hydrogenations each happen via a different route: the first hydrogenation occurs in the plasma, (ii) $N + H \rightarrow NH$, the second hydrogenation follows an ER path, (iii) $NH + H^* \rightarrow NH_2^*$, and the last hydrogenation follows a LH path, (iv) $NH_2^* + H^* \rightarrow NH_3$. Vibrational excitations of N_2 were included in this model up to the eighth excited level and corresponding catalytic dissociation rates were defined based on approximate sticking coefficients. Catalytic dissociation of vibrationally excited N_2 was found to be not as important as the reactions of plasma-generated radicals. While these results provide interesting kinetic insights, the model was limited by the assumed plasma conditions, the choice of catalyst and the simplified reaction kinetics.

In reality, a DBD plasma typically exhibits a filamentary character, consisting of microdischarge filaments and weaker plasma in between. However, depending on the conditions, more uniform (surface) discharges may also be present. Wang et al.[18] calculated that in packed bed DBDs (as typically used in plasma catalysis) the discharge mode is uniform when the dielectric constant of the packing is lower than 5, filamentary when the dielectric constant is higher than 1000, and the plasma exhibits a mixed mode for dielectric constants in between 5 and 1000. Support alumina has a dielectric constant of 9.3. It is unknown how much higher the dielectric constant is for alumina loaded with 10 wt % transition metals. Microdischarges were also found to be promoted by zeolites in the DBD, changing the IV characteristics of the plasma and enhancing NH_3 synthesis.[19] In addition, microporous phases, like zeolites and metalorganic frameworks (MOFs), can also improve diffusion of the plasma-activated species toward the active sites.[20,21]

For a realistic representation of plasma-catalytic NH_3 synthesis, different plasma conditions must be accounted for. Therefore, in this paper we discuss the surface kinetics, (i) in the microdischarges of a filamentary plasma, (ii) in between the microdischarges of a filamentary plasma, and (iii) in a uniform plasma. The densities of radicals and the vibrational distribution functions (VDF) are obtained from a plasma chemical kinetics model.[22] The surface reaction rates are determined via scaling relations and vibrationally enhanced dissociation of N_2 is simulated via an alpha-model, like in recent research by Mehta et al.[4] However, while Mehta et al.[4] assumed a theoretical VDF and did not include radical densities or ER reactions, our model accounts for different VDFs and includes radical densities and ER reactions. Results are studied over a wide range of transition metal catalysts and focus on comparing the impact of the different plasma species and their reactions.

Our models predict (i) that different vibrational distribution functions impact the choice of the optimal catalyst material, (ii) that ER reactions likely compete with and may have a greater impact on observed turnover frequencies than vibrational excitations, and (iii) that ER reactions likely decrease the sensitivity of observed turnover frequencies to the choice of catalytic material.

COMPUTATIONAL METHOD

A. Microkinetic Model of the Catalytic Reactions. We developed a mean-field microkinetic model[4,23,24] to simulate plasma-catalytic NH_3 synthesis. This model includes catalytic reactions of both plasma-generated radicals and vibrationally excited N_2 molecules. The rate equations of these catalytic reactions can be described as the time derivative of the surface coverages:

$$\frac{\partial \theta_i}{\partial t} = \sum_j c_{ij} r_j \tag{1}$$

where θ_i is the surface coverage of adsorbate i (defined as the total number of adsorbed species per total number of adsorption sites), c_{ij} is the stoichiometric coefficient for the adsorbate in

https://doi.org/10.1021/acssuschemeng.1c02713
ACS Sustainable Chem. Eng. 2021, 9, 13151−13163

Table 1. List of Surface Reactions Included in the Microkinetic Model[a]

thermal reactions	radical adsorption	Eley−Rideal (with H*)	Eley−Rideal (with N* or NH_x*)
$H_2 + 2* \rightleftharpoons 2H*$	$H + * \rightleftharpoons H*$	$H + H* \rightleftharpoons H_2$	$H + N* \rightleftharpoons NH*$
$N_2 + 2* \rightleftharpoons 2N*$	$N + * \rightleftharpoons N*$	$N + H* \rightleftharpoons NH*$	$H + NH* \rightleftharpoons NH_2*$
$N* + H* \rightleftharpoons NH*$	$NH + * \rightleftharpoons NH*$	$NH + H* \rightleftharpoons NH_2*$	$H + NH_2* \rightleftharpoons NH_3$
$NH* + H* \rightleftharpoons NH_2*$	$NH_2 + * \rightleftharpoons NH_2*$	$NH_2 + H* \rightleftharpoons NH_3$	$N + N* \rightleftharpoons N_2$
$NH_2* + H* \rightleftharpoons NH_3$			

[a]Details on the kinetic data are shown in the Supporting Information (section 1, Table S1 and S2).

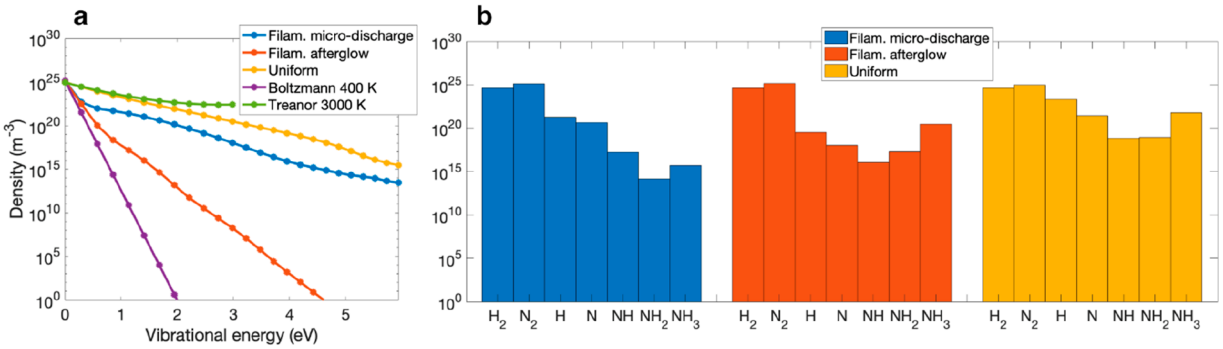

Figure 1. Calculated N_2 VDFs (a) and radical densities (b) in a DBD, in the microdischarges of a filamentary discharge (blue), in the afterglow in between these microdischarges (red), and in a uniform discharge (yellow). VDFs are compared with a Boltzmann distribution at 400 K (purple) and a truncated Treanor distribution at 3000 K (green).[4]

surface reaction j, and r_j is the rate (in coverage $^{-1}$) corresponding to this reaction, which is defined as

$$r_j = k_{j,f} \prod_s a_s^{c_{sj,f}} - k_{j,r} \prod_s a_s^{c_{sj,r}} \tag{2}$$

with $k_{j,f}$ and $k_{j,r}$ the forward and reverse reaction rate coefficients, a_s the activity of species s (equal to the coverage in the case of adsorbates and to the partial pressure, in bar, in the case of gas phase species),and $c_{sj,f}$ and $c_{sj,r}$ the stoichiometric coefficients of the reactants of the forward and the reverse reactions, respectively. Reaction rate coefficients $k_{j,f}$ and $k_{j,r}$ are calculated with harmonic transition state theory, using the Eyring-Polanyi equation:

$$k_{\mathrm{HTST}} = \frac{k_B T}{h} e^{\Delta S^{\circ\ddagger}/R} e^{-\Delta H^{\ddagger}/RT} \tag{3}$$

Here, k_B is the Boltzmann constant, h is Planck's constant, and $\Delta S^{\circ\ddagger}$ and $\Delta H^{\ddagger}$ are the entropy and enthalpy barriers to the transition state, respectively.

A set of rate equations was constructed to compute the reaction kinetics on the terrace sites of a range of transition metal catalysts in contact with an N_2/H_2 gas (plasma) mixture. The $\Delta H^{\ddagger}$ for the forward and backward reactions are related to the binding energy of N, E_b, through scaling relations built from DFT-computed reaction and activation energies tabulated in the CatApp database.[3,4,25] Reaction rate coefficients are assumed constant throughout the simulations;i.e.,reaction energies and barriers are assumed independent of previously adsorbed species (or thus possible changes in electronic structure because of them), as is commonly done in microkinetic modeling.[26] More details can be found in the Supporting Information (section 1 and Table S1). We solved the ordinary differential rate equations on the most noble catalyst (E_b = 3 eV, corresponding to Ag) until the surface coverage reached a steady state ($\partial\theta_i/\partial t = 0$ for all species i). In subsequent steps, we decreased E_b in increments of −0.01 eV until E_b = −1.5 eV (close to Re, E_b = −1.4 eV). During each iteration, new reaction barriers and the corresponding reaction rate coefficients were calculated, and the steady state of the previous step was used as a guess to solve for an algebraic solution. This solution was inserted back into the rate equations to obtain steady state turnover frequencies (TOFs).

We note that all catalytic reactions (see Table 1, discussed in the results) are treated as reversible. As shown in Figure 1b, further on, and listed in Table S3 of the Supporting Information, NH_3 concentrations are nonzero throughout the calculations of the TOFs in sections 1.2 and 1.3. Also assuming a nonzero NH_3 pressure in section 1.1, would lower the net TOFs but not change the calculated trends. Nonetheless, net catalytic NH_3 synthesis rates are positive at all conditions.

The plasma can sometimes also induce structural modifications of the catalyst that are very complex and diverse in nature and can impact the process. Such interactions are often impossible to implement in zero-dimensional models and would require a lot of additional DFT calculations of the partaking atoms and molecules in different adsorption sites.[27]

B. Plasma Chemical Kinetics Model. We use the output of our previously developed plasma chemical kinetics model of a DBD[22,28] as input to the microkinetic model. The plasma chemical kinetics DBD model uses the ZDPlasKin module[29] which solves the continuity equation for species in complex chemistries. Analogous to the rate equations above, the time derivative of the species densities is equal to the sum of reaction rates:

$$\frac{\partial n_i}{\partial t} = \sum_j c_{ij} r_j \tag{4}$$

where n_i is the density of species i, c_{ij} is the stoichiometric coefficient of the species in reaction j, and r_j is the reaction rate (in m^{-3} s^{-1}), defined as

https://doi.org/10.1021/acssuschemeng.1c02713
ACS Sustainable Chem. Eng. 2021, 9, 13151−13163

$$r_j = k_j \prod_s n_s^{c_{sj}} \quad (5)$$

with k_j the rate coefficient, n_s the species density of reactants s and c_{sj} the stoichiometric coefficient of the reactants in the reaction.

ZDPlasKin is coupled to BOLSIG+,[30] which calculates the electron energy distribution function at specified reduced electric fields (i.e., ratio of electric field over gas number density). In our plasma chemical kinetics model, we self-consistently calculate the reduced electric field from a specified power density. The power density conditions determine the described plasma behavior.

To mimic the conditions of DBD plasmas, we defined time-dependent periodically pulsed power density functions. The power density in between those pulses (i.e., microdischarges) was nonzero and significantly influenced the outcome of the calculations. By changing the significance of the microdischarges and the plasma in between them, we could describe both filamentary DBDs (most common in N_2/H_2 mixtures) and also a more uniform regime, in which the microdischarges are of lesser importance,[28] which could be relevant to packed bed DBDs, with packing beads of low dielectric constant.[18] Different power density profiles were used, mimicking both filamentary and more uniform (packed bed) DBDs, to determine gas phase compositions of radicals in actual plasma conditions, as well as the vibrational distribution function (VDF). Both the microdischarges (strong plasma) and their afterglows (weak plasma) in a filamentary plasma are considered. Those conditions correspond to a maximum power density of 2.464×10^{12} W/m^3 and to a minimum power density of 2.464×10^6 W/m^3, respectively. The corresponding instantaneous power is 1232 W and 1.232 mW, respectively. Those pulses typically yield reduced electric fields between 10 and 100 Td. In addition, we consider a uniform plasma in which the minimum power density is 3 orders of magnitude higher, 2.360×10^9 W/m^3 compared to 2.464×10^6 W/m^3, corresponding to an instantaneous power of 1.180 W. In this uniform plasma case, the microdischarges are still present and are similar to the filamentary plasma (i.e., 2.360×10^{12} W/m^3 compared to 2.464×10^{12} W/m^3, corresponding to an instantaneous power of 1180 W), but they did not influence the VDF or species density evolution in a significant way. In this case the reduced electric field is between 20 and 100 Td. Throughout the simulations, the gas temperature was kept constant at 400 K (which is a typical temperature for DBD reactors) and the gas phase composition was a 3:1 N_2/H_2 plasma at atmospheric pressure. We refer to van 't Veer et al.[28] for more details.

RESULTS AND DISCUSSION

We performed microkinetic simulations for different plasma conditions, characteristic of a DBD plasma. We show the results of a DBD operating in a filamentary regime and in a uniform regime. As mentioned above, a filamentary regime exhibits microdischarges with a high instantaneous power (in the order of 1.2 kW), while the plasma in between the microdischarges is characterized by a much lower power (in the order of 1.2 mW).[28] The latter is referred to as the afterglow of the microdischarges. During the afterglows, the radical densities and VDF are very different from the densities and VDF throughout the microdischarges. In the case of a uniform plasma, the power deposition remains approximately constant over time and so do the radical densities and VDF. These differences in plasma characteristics also translate to different surface kinetics.

As we consider an alumina packing (with dielectric constant of ~9.3, loaded with transition metal catalysts), the plasma operates in a mixed mode of uniform (surface) and filamentary discharges, so we applied different power density profiles, mimicking both uniform and filamentary (packed bed) DBDs. In addition, this makes our model generic, applicable to various conditions and DBD operation modes. It is the aim of this paper to show the total NH_3 turnover frequency (TOF) in these plasma regimes, to elucidate the mechanisms and the kinetics of the reactions at play and compare the obtained insights with previous observations and conclusions in literature.

It should be noted that when considering the microdischarges (or filaments) and their afterglows in a filamentary plasma, the radicals created in the microdischarges may diffuse to the neighboring afterglow zones and influence the reactions there. However, this effect cannot be captured yet in our microkinetic model, because we use the plasma species densities as input from the plasma kinetics model by van 't Veer et al.,[22] and the latter is a 0D or global plasma model, which does not capture spatial effects such as diffusion. The latter would require higher dimensional models, but capturing the filamentary behavior in computational fluid dynamics plasma models is very complex.

In the global plasma model by van 't Veer et al., a temporal definition of the afterglow is used; i.e., the afterglow is defined as the period after extinction of a microdischarge. Van 't Veer et al. has shown that the lifetimes of radicals created in the microdischarges are typically large enough (order of 30 ms) to last until the afterglow. The VDF in the microdischarges of the filamentary plasma relaxes back to the VDF in the afterglows in approximately 1 ms, i.e., on a time scale much longer than the microdischarge duration (ns time scale).

1. NH_3 Turnover Frequency. In the following sections, we apply our microkinetic model to the metal terrace sites in contact with the plasma composition found (i) in the microdischarges (at maximum power) of a filamentary plasma, (ii) in the end of the afterglow in between these microdischarges, and (iii) in a uniform plasma, as calculated previously by van 't Veer et al.[22] We will first show the impact of the different VDFs and afterward introduce the radical reactions. The introduction of radical reactions will be performed in two steps, i.e., first radical adsorption and second ER reactions.

1.1. Impact of Vibrational Distribution Functions (VDFs). In this section we study the effect of different VDFs on the NH_3 TOF. We show the results from thermal catalysis and the impact of a truncated Treanor distribution as previously modeled by Mehta et al.[4] Furthermore, we introduce the VDFs as calculated by van 't Veer et al.,[22] for a filamentary plasma (both inside and in between the microdischarges) and for a uniform plasma.

The elementary reactions considered in this section are listed in the first column of Table 1. These are the traditional reactions for thermal catalysis and are also the only reactions in *plasma-enhanced catalytic* NH_3 synthesis, where the plasma only aids in lowering the barrier of the catalytic dissociation of the reactant molecules and thus increases the rate of the first two reactions in the first column.

The reaction barriers for the LH reactions (Table 1, column 1) on the metal terrace sites were obtained through scaling relations, as established by previous works[3,4] based on DFT-computed results listed in the CatApp database.[25] The used scaling relations are discussed in more detail in section 1 of the Supporting Information.

https://doi.org/10.1021/acssuschemeng.1c02713
ACS Sustainable Chem. Eng. 2021, 9, 13151−13163

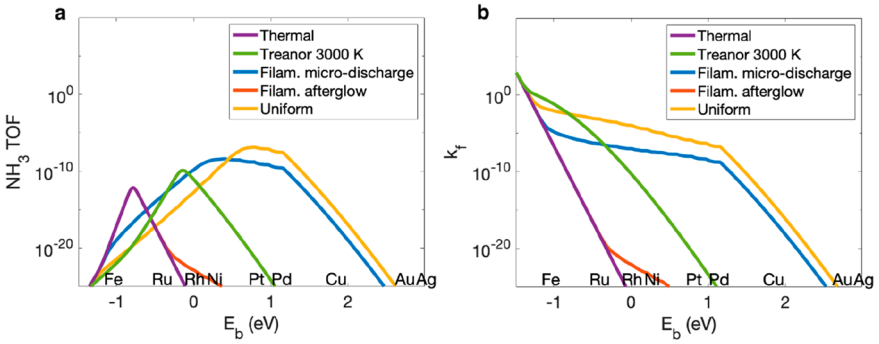

Figure 2. (a) Calculated NH_3 TOF at 400 K and 1 bar in vibrationally enhanced catalysis and (b) calculated N_2 dissociation rate coefficient, as a function of N* binding energy, for the metal terrace sites, (i) in thermal catalysis, thus no vibrational excitation (purple line), (ii) with a VDF following a Treanor distribution at 3000 K (green line), (iii) with a calculated VDF during the microdischarges of a filamentary plasma (blue line), (iv) with a calculated VDF during the afterglow of the microdischarges of a filamentary plasma (red line), and (v) with a calculated VDF inside a uniform plasma.

Vibrational excitation of N_2 is assumed to lower the dissociative adsorption barrier following an α model:[4]

$$k_\nu = \frac{k_B T}{h} e^{\Delta S^{\circ\ddagger}/R} e^{-\Delta H^{\ddagger}/RT} e^{\alpha E_\nu/RT} \quad (6)$$

$$k = \sum_\nu p_\nu k_\nu \quad (7)$$

Here, k_ν represents the reaction rate coefficient of an N_2 molecule in the νth vibrational level with energy E_ν, k_B is the Boltzmann constant, h is Planck's constant, $\Delta S^{\circ\ddagger}$ and $\Delta H^{\ddagger}$ are the entropy and enthalpy barriers with respect to the transition state, and k is the ensemble averaged reaction rate coefficient of vibrationally excited N_2 following a VDF defined by the probabilities p_ν. The α parameter gives a measure of the efficiency of the vibrational energy to lower the reaction barrier. To date, no exact expressions for α are known. An approximate formulation for vibrationally enhanced dissociation of diatomic molecules was provided by Fridman, who related α to the forward and backward activation energies, E_a^f and E_a^b.[31]

$$\alpha = \frac{E_a^f}{E_a^f + E_a^b} \quad (8)$$

Conceptually, if E_a^f is zero, the reaction is diffusion limited and there is no enthalpy barrier to overcome, so α is zero. On the other hand, if E_a^b is zero, the reaction is purely enthalpy limited and benefits maximally from the provided vibrational energy, thus α equals one.

The VDFs studied in this section are shown in Figure 1(a). The first VDF, represented by the purple line, represents a Boltzmann distribution at 400 K (i.e., the assumed gas temperature) as reference. The green line represents a Treanor distribution at 3000 K, truncated at the 11th energy level, as previously applied by Mehta et al.[4] The blue, red, and yellow VDFs are calculated with our plasma kinetics model.[28] These are the VDFs from the microdischarges of a filamentary plasma (T_{vib} = 597 K), in between two such microdischarges (i.e., afterglows) with T_{vib} = 554 K, and from a uniform plasma (T_{vib} = 2623 K), respectively.

In Figure 2(a) we show the calculated NH_3 TOFs as a function of the N* binding energy for the different VDFs. The purple line displays the well-established volcano behavior observed in thermal catalysis. The green line indicates the effect of a truncated Treanor distribution at 3000 K, as previously studied by Mehta et al.[4] In this case, vibrational excitations have two important effects on the TOF. First, the TOF is increased on the noble side (right side) of the thermal volcano, where the NH_3 synthesis is rate-limited by N_2 dissociation. Second, the maximum TOF is higher than the maximum thermal TOF, by a factor of 1.84×10^2. The higher vibrational energy levels are sufficiently populated for the N_2 dissociation rate on Rh to exceed the N_2 dissociation rate on the thermally optimal catalyst (in between Fe and Ru, at −0.9 eV). On Rh, the TOF benefits from both a higher dissociation rate due to plasma excitation and a higher product desorption rate due to the more noble catalyst material.

However, the TOFs depend strongly on the assumed VDFs, and the Treanor distribution is only a rough approximation of the actual VDF in a filamentary plasma, as used for NH_3 synthesis, as is clear from Figure 1(a) above. For instance, in the microdischarges of the filamentary plasma, the vibrational temperature remains relatively low (at 597 K) but with a non-negligible population beyond the 11th level. In this case, the TOF plot (blue curve) looks much different than the thermal volcano or the volcano corresponding to the Treanor distribution. The volcano plot has become much wider and despite the lower vibrational temperature, the TOF during the microdischarges exceeds on many catalysts the TOF obtained from a Treanor distribution. Only in between Ru and Rh does the Treanor distribution perform slightly better than the VDF of the microdischarges. Beyond the 11th level, the populations of the Treanor distribution are zero and the populations of the VDF of the microdischarges are higher. Higher levels of excitation allow more noble catalysts to produce NH_3 and the volcano stretches out to the right. These results show how important the population of the higher levels is, compared to the vibrational temperature which is only a measure of the population of the ground state and the first excited state.

The highest TOFs are obtained from the VDF of the uniform plasma, despite the vibrational temperature (2623 K) being somewhat lower than the Treanor distribution. This is because the distribution is not truncated. The population of the higher levels shifts the volcano to more noble catalysts with a maximum around Pt, a factor 10^3 higher compared to the Treanor distribution.

In Figure 2(b), we depict the forward rate coefficients of N_2 dissociation as a function of the N* binding energy for each of the assumed VDFs. On the far-right side of the graphs, the dissociation barrier is highest and vibrational energy contributes maximally to lowering this barrier. When moving toward less noble catalysts, the dissociation barrier decreases and the rate

https://doi.org/10.1021/acssuschemeng.1c02713
ACS Sustainable Chem. Eng. 2021, 9, 13151−13163

coefficient follows a plateau, where gradually the contribution of the higher levels is canceled. Indeed, if the energy of the nth level (multiplied by the α parameter) would be higher than the dissociation barrier, E_a, the barrier is lowered by E_a and not by αE_n. In this regime, the vibrational energy can thus not fully contribute to the catalytic dissociation. On even less-noble catalysts, the α parameter has become much smaller and most of the vibrational energy goes unused, causing the dissociation rate coefficient to fall back to the thermal dissociation rate coefficient.

Figure 2(a) highlights the potential of plasma catalysis by means of vibrational excitation but also shows the importance of choosing the appropriate catalyst. It is clear that vibrational excitation can enhance the catalytic NH_3 TOF (i.e., from 10^{-12} s^{-1} in thermal catalysis to 10^{-9} s^{-1} inside the microdischarges of a filamentary plasma and 10^{-7} s^{-1} inside a uniform plasma). However, it should be noted that the best thermal catalyst performs better in thermal catalysis than when put in contact with the Treanor distribution or the VDF of the uniform plasma. In these cases, the product desorption on the thermal catalyst is not fast enough to deal with the enhanced dissociation of the reactants. Plasma-enhanced catalytic NH_3 synthesis, which takes advantage of vibrational excitation of N_2, therefore requires careful choice of the catalyst material as a function of the plasma conditions.

1.2. Impact of Radical Adsorption. We now add the direct adsorption of plasma-generated radicals onto free surface sites (Table 1, column 2). In this case, the plasma can provide a new initializing adsorption step, but the subsequent surface reactions follow the LH mechanisms from the thermal conditions. Radical adsorption is assumed to proceed without an enthalpy barrier and is rate-determined by the assumed complete loss of translational entropy associated with moving from the gas phase to the adsorbed state. Radical adsorption rates are thus calculated as follows:

$$r_{ads} = \frac{k_B T}{h} e^{-S_i^\circ/R} p_i \theta_* \quad (9)$$

with S_i° the standard entropy of radical 'i' at temperature T, p_i the pressure of radical 'i', and θ_* the fraction of free surface sites.

We show the results for the radical densities calculated inside the microdischarges and afterglows of a filamentary plasma and inside a uniform plasma. These densities are plotted in Figure 1(b), and the exact values are tabulated in Table S3 of the Supporting Information. These radicals are predicted not only by modeling to be important in DBDs but also by optical emission spectroscopy.[32]

Figure 3 depicts the NH_3 TOFs, analogous to the ones shown in Figure 2(a), but now including the effect of vibrationally excited N_2 as well as plasma-generated radical adsorption. The allowed reactions are listed in columns 1 and 2 of Table 1. The plasma-catalytic TOF curves now look significantly different than in the previous section. In each of the cases, the maximum TOF can be observed on the most noble catalysts. With radical adsorption happening fast, the NH_3 production is rate-limited by product desorption, which is fastest on noble catalysts. In the afterglows of a filamentary discharge, the maximum TOF is already reached around Cu, while in the microdischarges the maximum is reached around Au, and in the uniform plasma, the maximum is not yet reached within the range of N* binding energies examined. The afterglows of a filamentary discharge contain the lowest radical densities of the three cases (cf. Figure 1(b)) and product desorption on catalysts on the right side of

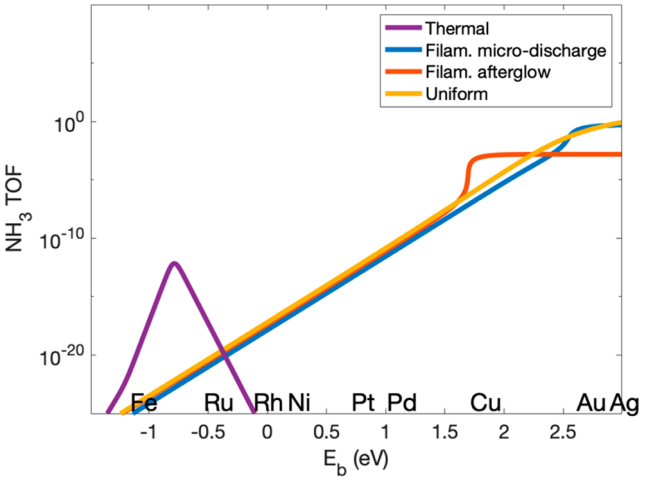

Figure 3. Calculated NH_3 TOF as a function of the N* binding energy, for the metal terrace sites at 400 K and 1 bar, (i) in thermal catalysis, thus no vibrational excitation and no radicals (purple line), (ii) inside the microdischarges of a filamentary plasma (blue line), (iii) during the afterglows of a filamentary plasma (red line), and (iv) inside a uniform plasma (yellow line). Calculations include the reactions in columns 1 and 2 of Table 1.

Cu is already happening faster than radicals can adsorb. NH_3 production is then rate-limited by radical adsorption, which is assumed barrierless on each catalyst and therefore has a constant rate beyond this point. For the microdischarges and the uniform plasma, the same trend holds, but the plateau is found at higher N* binding energies, because the adsorption rates are higher due to higher radical densities.

Despite having different radical densities in the gas phase, the TOFs during the microdischarges of a filamentary plasma, during the afterglows of a filamentary plasma, and during a uniform plasma are identical, until the TOFs of the afterglows reach the plateau around Cu. This can be explained by the fact that radical adsorption is not rate limiting and, in each case, the same desorption reaction is limiting the NH_3 TOF, namely, $2N^* \rightarrow N_{2(g)}$.

We also note that the TOF on the thermally optimal catalyst (in between Fe and Ru) is again significantly lower under plasma conditions than in thermal conditions. Around these N* binding energies, product desorption is too low to counter the radical adsorption rate, and the buildup of N* species inhibits further hydrogenation toward NH_3.

1.3. Impact of Eley–Rideal Reactions. We now include the ER reactions of plasma-generated radicals with adsorbed species (cf. Table 1, columns 3 and 4). Unlike in the previous sections, these reactions do not require the involving species to be simultaneously adsorbed on the catalyst and are thus not inhibited by competitive adsorption.

Throughout this section, ER reactions are considered to have no enthalpy barrier and are thus only limited by the entropy loss going from a gas phase state to a surface state. To support this claim, we provide in the Supporting Information the DFT-calculated potential energy surfaces of three ER reactions, i.e., $N + N^* \rightarrow N_{2(g)}$, $H + H^* \rightarrow H_{2(g)}$, and $N + H^* \rightarrow NH^*$, on Ru, Ni, and Cu (see section 3 of the Supporting Information, Figures S1–S3). To account for the limitations of DFT calculations, we present a sensitivity analysis in the next section, to study the impact of assumed ER rates on the NH_3 TOFs.

https://doi.org/10.1021/acssuschemeng.1c02713
ACS Sustainable Chem. Eng. 2021, 9, 13151–13163

In Figure 4 we plot the calculated NH_3 TOFs, analogous to Figures 2 and 3, now including all the reactions listed in Table 1.

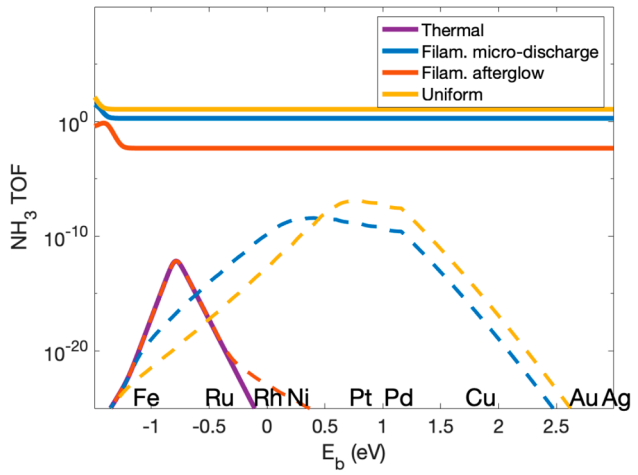

Figure 4. Calculated NH_3 TOF as a function of the N* binding energy, for the metal terrace sites at 400 K and 1 bar, (i) in thermal catalysis, thus no vibrational excitation and no radicals (purple line), (ii) inside the microdischarges of a filamentary plasma (blue line), (iii) during the afterglows of a filamentary plasma (red line), and (iv) inside a uniform plasma (yellow line). Calculations include all the reactions in Table 1. The dashed lines represent the NH_3 TOF when only including vibrational excitation (identical to Figure 2).

The dashed lines show the TOFs when only vibrational excitations are considered (i.e., no radical reactions, identical to the results shown in Figure 2), for easy comparison between the two plasma effects.

In the LH plus radical adsorption model, in which ER reactions are excluded, the TOF was highest on the noble catalysts. After introduction of barrierless ER reactions, this variation vanishes and the TOF is invariant to material. In the previous case, surfaces become completely covered with adsorbates and rates are slow due to the absence of free sites for subsequent reactions. However, because the ER reactions lead to products without the intervention of free surface sites, rates on the non-noble side of the plot increase.

In each of the three cases, the NH_3 production is rate-limited by radical reactions, either adsorption reactions (Table 1 column 2) or ER reactions (Table 1 columns 3 and 4). This is also confirmed by the fact that the TOFs are equal to the plateaus observed in the previous section (Figure 3). The kinetics will be discussed further in section 2 (Reaction Mechanisms and Kinetics).

Figure 4 also shows the calculated NH_3 TOFs as obtained from the models with only vibrational excitations of N_2 (dashed lines, identical to Figure 2). In the three cases, radical reactions have a much larger impact on the total NH_3 TOF than vibrational excitation. In each case, the characteristic volcano behavior of thermal catalysis is not observed.

1.4. Sensitivity Analysis of the Eley–Rideal Barriers. In the previous section, we assumed that the surface is 100% effective in dissipating adsorption energy associated with radical reactions (i.e., acts as a perfect third body), effectively cooling and concentrating the radicals. In this section, we introduce an additional free energy barrier to the ER reactions to explore the consequences of kinetic limitations of these reaction steps. We do so by applying an artificial Boltzmann factor to the rates in two steps: (i) gradual increase of the barriers of the reactions in column 3 of Table 1 and (ii) gradual increase of the barriers of the reactions in column 4 of Table 1. In both cases the remaining ER reactions are assumed to be barrierless. The reaction rate coefficients, k_{ER}, are calculated with the formula

$$k_{ER} = k_{ER,0} e^{-E_{ER}/RT} \quad (10)$$

Here, $k_{ER,0}$ represents the maximum rate coefficient, assuming radical reactions are barrierless and the exponential factor is the Boltzmann factor corresponding to an assumed ER barrier, E_{ER}.

E_{ER} is assumed constant in the entire range of binding energies, i.e., catalyst materials. Due to the similarity of the reactions in column 3 (all ER reactions involving H*), each one of these reactions is assumed to have the same enthalpy barrier. Analogously, the reactions in column 4 all involve N* or NH_x* and are therefore also assumed to proceed with the same enthalpy barrier. We emphasize that in each case there is also an entropy barrier, which depends on the entropy of the gas phase reactant. For this reason, each of the reactions in column 3 still has a unique reaction rate coefficient. Similarly, reaction 4 in column 4 has a different rate coefficient than the other three reactions.

We show here the results for the microdischarges of a filamentary plasma and refer to the Supporting Information for the results on the afterglows of the filamentary plasma and on the uniform plasma (section 4 of the Supporting Information, Figures S4 and S5).

Figure 5 illustrates how different ER reaction barriers impact the NH_3 TOF, for the reactions in Table 1, column 3 (panel a), column 4 (panel b), and columns 3 and 4 together (panel c).

From Figure 5a, it is clear that upon changing the barriers of the ER reactions in column 3 of Table 1, the NH_3 TOF remains almost unchanged. In the maximum rate case, the ER reaction N + H* → NH* is rate limiting. When this reaction rate is decreased, another ER reaction (from column 4), i.e., H + N* → NH*, takes its place, with a rate of about a factor 3 smaller. More details on the reaction mechanisms are discussed in section 2 (Reaction Mechanisms and Kinetics). Figure 5b shows that the reaction barriers of the ER reactions in column 4 of Table 1 have a much greater impact on the NH_3 TOF. Without these reactions, the hydrogenations toward NH_3 become more difficult and the catalyst suffers from poisoning by NH_x species.

From a chemical perspective, the reactions in column 3 of Table 1 are more likely slower than the reactions in column 4. For N + H* → NH* to proceed, for example, the N atom would have to take the place of the H atom on the surface, because NH* is attached to the surface via the N atom instead of the H atom. However, Figure 5a shows that overall TOFs are less sensitive to this rate.

Lastly, Figure 5c reports the NH_3 TOF when all ER barriers (columns 3 and 4 in Table 1) are gradually increased. In these calculations all ER enthalpy barriers are assumed equal and are gradually increased from 0 to 5 eV. The results are similar to Figure 5b for the lower energy barriers, but with less poisoning at the higher energy barriers. As the barriers increase, the TOF converges to the TOF of the blue line in Figure 3, where only reactions from columns 1 and 2 in Table 1 are allowed.

Note that the results for the afterglows of the filamentary plasma and for the uniform plasma exhibit the same behavior (see Figures S4 and S5 in the Supporting Information).

In conclusion, the ER reactions in column 3 (N + H* or NH_x + H*) are relatively insignificant, as long as the ER reactions in

https://doi.org/10.1021/acssuschemeng.1c02713
ACS Sustainable Chem. Eng. 2021, 9, 13151−13163

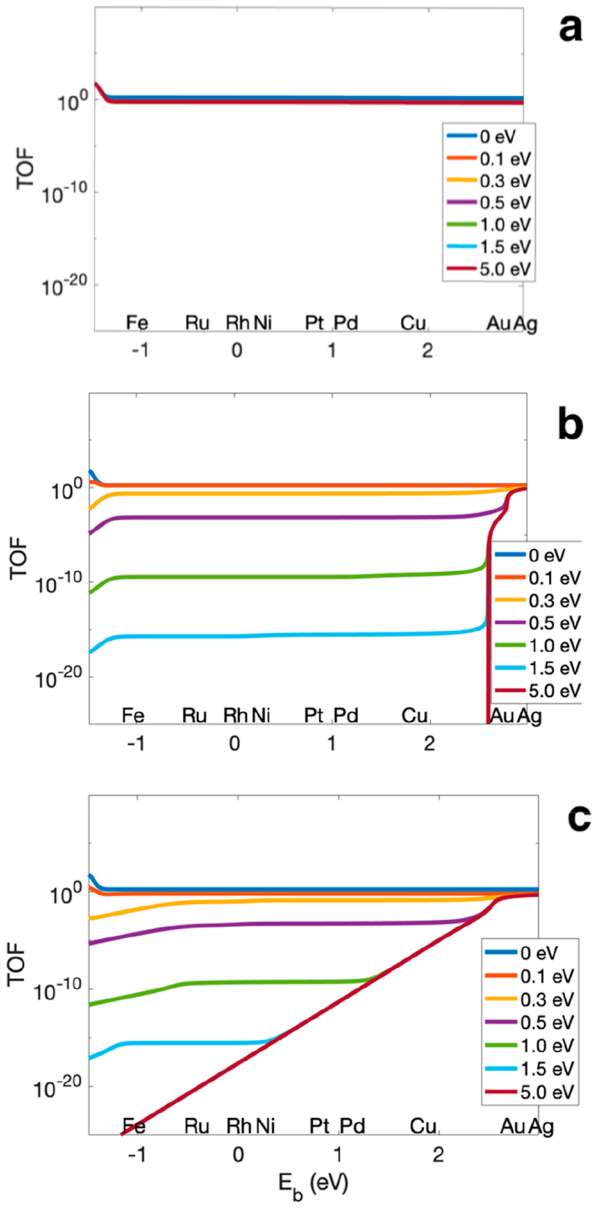

Figure 5. Calculated NH_3 TOF as a function of the N* binding energy, for the metal terrace sites, at 400 K and 1 bar, inside the microdischarges of a filamentary plasma for different barriers of the ER reactions, (a) in Table 1, column 3, (b) in Table 1, column 4, and (c) in Table 1, columns 3 and 4 together.

column 4 (H + N* or H + NH_x*) can continue to drive the production forward. Without the reactions in column 4, the N + H* and NH_x + H* reactions will quickly deplete the H* coverage. This poisons the surface with NH_x* species, which have no further way to hydrogenate, as H adsorption is not possible due to the poisoning and H + NH_x* reactions are not allowed. Further, ER reactions seem to mostly impact the kinetics on the non-noble catalysts, while the TOF on the noble catalysts remains unchanged. Moreover, without ER reactions, the TOF on the non-noble catalysts becomes negligible, e.g., 10^{-20} s^{-1} on Ru in Figure 5c (5 eV barrier). Figure 2 (blue line) showed that when only vibrational excitation is assumed (i.e., a microdischarge without including radicals), the TOF on Ru reached a value of up to 10^{-9} s^{-1}.

Within our model assumptions, the ER reactions are expected to contribute more to observed TOFs than do LH steps on the non-noble catalysts. The importance of ER reactions is expected to be great at the high radical densities typically present in DBD plasmas.[17,22,28] To what extent plasma-activated species can penetrate the pores of the catalyst and interact with the active metal sites and how plasma-activated species interact with support materials can be an important descriptor for efficient catalyst design. The mesoporous nature of zeolites and MOFs retains specific interest to enhance diffusion of plasma species and/or alter plasma characteristics that could help further optimization of the technology.[19−21]

2. Reaction Mechanisms and Kinetics. The previous section focused on the total NH_3 TOF in a filamentary and a uniform plasma, to elucidate the relative contributions of various pathways to the total TOF. In this section, we discuss in more detail the full reaction pathways, identify the bottle necks and formulate the resulting reaction rate equations. For this discussion, all the reactions in Table 1 are included and ER reactions are assumed to occur at maximum possible rate, as in Figure 4. In this discussion we will focus on the microdischarges of the filamentary plasma. Because our model predicts that the reaction mechanisms are the same among the various non-noble catalysts on the one hand, and the noble catalysts on the other hand, we will show the results on Ru as an example of a non-noble catalyst and Ag as an example of a noble catalyst.

The density of plasma species and the VDF of N_2 in the microdischarges, at maximum instantaneous power, as obtained from the simulations by van 't Veer et al.,[22] are shown in Figure 1. At the maximum power, N and H are the most important radicals in the plasma. The density of N is about 10^3 times higher than NH, 10^6 times higher than NH_2, and about 10^5 times higher than NH_3. The vibrational temperature, defined based on the ratio of the populations of the first exited state and the ground state, is 597 K.

In Figure 6, we show net rates along the various parallel NH_3 synthesis pathways during the microdischarges of a filamentary

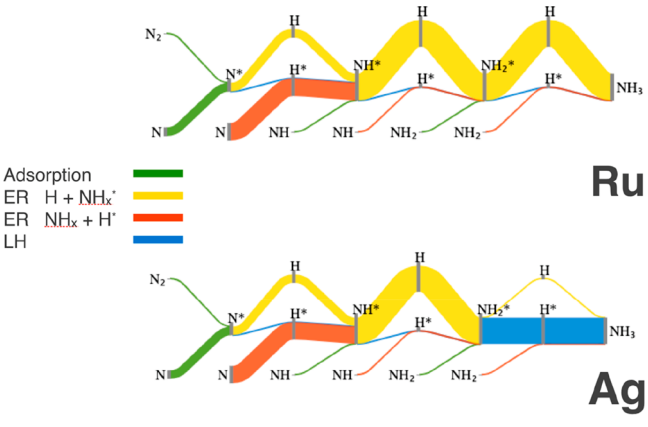

Figure 6. Reaction flow diagrams for plasma-catalytic NH_3 synthesis on a non-noble catalyst (Ru) and a noble catalyst (Ag), presenting the relative weight of the various reaction rates, in a filamentary DBD, during the microdischarges.

DBD, for a non-noble catalyst (Ru) and a noble catalyst (Ag). These flow diagrams show the net reaction rates of each reaction in the chemistry set. We refer to the Supporting Information (Figure S6) for the exact values of the reaction rates as a function

https://doi.org/10.1021/acssuschemeng.1c02713
ACS Sustainable Chem. Eng. 2021, 9, 13151−13163

of the N* binding energy, and the ratio of the contribution of ER and LH reactions (Table S5).

On the non-noble catalyst (Ru), the primary source of NH_3 is the ER mechanism of $NH_2^* + H_{(g)}$. The required NH_2^* is produced from the ER reaction $NH^* + H_{(g)}$. The NH* in this case is mainly produced from the ER reaction $N_{(g)} + H^*$ (see Figure 6), which is the rate limiting step in this regime. On the non-noble catalysts, the net rate of NH_3 synthesis can be written as

$$\text{rate} = k_{ER} p_N \theta_H \tag{11}$$

where k_{ER}, p_N, and θ_H stand for the rate coefficient of N + H* → NH*, the N radical pressure in the plasma, and the fraction of adsorbed H, respectively.

In section 1.4 (Sensitivity Analysis of the Eley−Rideal Reaction Barriers), we showed that if N + H* → NH* is slow, ER reactions with H + N* or H + NH_x* would replace it. In that case, the path would be N + * → N*, followed by H + N* → NH*. When N + H* is allowed, the reaction rate is about a factor 2 larger than H + N*.

On the noble catalyst (Ag), NH_3 is primarily produced through the LH mechanism of $NH_2^* + H^*$ (the ER reactions $NH_2 + H^*$ and $H + NH_2^*$ are a factor 10^6 less important). The required NH_2^* is produced from the ER reaction $NH^* + H_{(g)} \rightarrow NH_2^*$, while the NH* is obtained via two possible ER reactions, i.e., $N^* + H_{(g)}$ and $N_{(g)} + H^*$. For both of these ER reactions, the source of N are the plasma-generated radicals that either adsorb on a free site (N + * → N*) before subsequent hydrogenation or are directly reacting with adsorbed H*. On the most noble catalysts, the H* coverage drops and the former reaction contributes more than the latter and will be the rate limiting step. The NH_3 TOF is thus directly proportional to the partial pressure of the N radicals in the plasma and the net rate of NH_3 synthesis can be written as

$$\text{rate} = k_{ads} p_N \theta^* \tag{12}$$

where k_{ads}, p_N, and θ^* stand for the rate coefficient of N radical adsorption, the N radical pressure in the plasma and the fraction of free surface sites, respectively. The rate of radical adsorption of N followed by ER hydrogenation, is about a factor three higher than for the other ER reaction, N + H* → NH*, because θ^* and θ_H are approximately 0.75 and 0.25, respectively. On even more noble catalysts, θ_H would be even lower, and the direct ER route N + H* → NH* would cancel entirely.

According to the classification by Rouwenhorst et al.,[14] both on the noble and the non-noble catalysts, the plasma-catalytic NH_3 synthesis can be called *plasma-enhanced semicatalytic*, i.e., dissociation of N_2 occurs in the plasma, while H_2 dissociation, as well as subsequent hydrogenation of N happens at the catalyst surface. In other words, the catalytic dissociation of H_2 on all catalysts is (slightly) faster (2.92×10^2 s^{-1}) than plasma dissociation of H_2 followed by radical adsorption of H (2.77×10^2 s^{-1}), while the catalytic dissociation of N_2 on the catalyst surface is slower than plasma dissociation followed by radical adsorption or ER reactions, for all catalyst materials investigated.

We note that rates (11) and (12) are identical to each other (as also tabulated in Table 2), because k_{ads} and k_{ER} are both equal to $k_B T/h \exp(-S^\circ_{N(g)})$, enthalpy barriers are in both cases 0, and $\theta^*_{noble} = \theta_{H,non\text{-}noble} = 1$. This means that in a plasma regime where the catalytic dissociation of N_2 is negligible compared to dissociation in the plasma phase, followed by radical adsorption and/or ER reactions, the catalyst material has no impact on the TOF of NH_3, as demonstrated in the previous section, in Figure 4.

Table 2. Reaction Rate Equations in a Filamentary Plasma in the Micro-discharges and the Afterglows on Ru and Ag and Reaction Rate Coefficient of the Rate Limiting Step

Ru	rate = $k_{ER} p_N \theta_H$
Ag	rate = $k_{ads} p_N \theta^*$
$k_{ER} = k_{ads}$	$k_B T/h \exp(-S^\circ_{N(g)})$

We emphasize that these results correspond to plasmas operating at around 400 K. At higher temperatures the transition metal catalysts become more active and could change the reaction pathways and kinetics. We refer to section 8 of the Supporting Information, for a discussion of reaction mechanisms for a filamentary plasma operating at 700 K. In summary of these results, LH reactions are found to be more important than ER reactions at higher temperature. However, adsorption of N atoms from the plasma is still more important for NH_3 formation than N_2 dissociation at the catalyst surface, explaining why the radical TOFs are still higher than the TOFs from vibrational excitation (cf. Figure S9 in the Supporting Information).

van't Veer et al. recently reported that in a filamentary plasma, NH_3 is produced by recombination in the afterglow, while the obtained NH_3 is partly destroyed again during the micro-discharges until an equilibrium conversion has been established.[22] Because electron impact dissociation of the produced NH_3 is inevitable in a plasma environment, the ultimate aim in plasma catalysis is to increase the production terms in order to increase the conversion. From this perspective, the results shown above also show the advantage of plasma-catalytic NH_3 synthesis over homogeneous plasma NH_3 synthesis. The introduction of radical recombination reactions breaks down the detailed balance of the thermal process because the reverse reactions (catalytic dissociation followed by desorption of one of the radicals) are nigh impossible due to the high barriers. So, while radical recombination toward NH_3 is quickly happening at the catalytic surface, NH_3 dissociation is happening much more slowly. On the noble catalysts this is explained by the high activation barrier of NH_3 dissociation, while on the non-noble catalysts this is due to the lack of free sites caused by the adsorption of radicals. Mehta et al.[6] showed that the introduction of plasma-activated reactions without a reverse reaction could lead to conversion beyond the thermal limits. However, while the inclusion of a surface can improve the conversion, within our model assumptions, it seems not to matter which transition metal is used, as all transition metals seem to perform equally well under these conditions and preference for application can be decided based on material cost and durability.

We acknowledge that the list of elementary reaction steps in this model (cf. Table 1), for plasma-catalytic NH_3 synthesis, is not exhaustive and that the complex plasma speciation allows for many more possible steps. The given list includes the elementary steps that are generally considered to be dominant in thermal catalysis, as well as radical adsorption reactions and Eley−Rideal reactions that were found or suggested to be important in previous experimental and modeling studies on plasma catalysis, as discussed in the next section, Insight of Our Models beyond the Current State of Knowledge. These studies show that experimental analysis of reaction pathways in plasma catalysis is very complex and not very decisive. Nevertheless, our model

https://doi.org/10.1021/acssuschemeng.1c02713
ACS Sustainable Chem. Eng. 2021, 9, 13151−13163

results both agree with and expand the conclusions and insights in the current state-of-the-art.

3. Insight of Our Models beyond the Current State of Knowledge. In this section, we revisit the current literature and compare the obtained insights from our models with previously reported trends and concepts.

Mehta et al.[4] predicted a vertical (higher) and horizontal (more noble) shift of the observed volcano when introducing vibrational excitation of N_2 compared to thermal catalytic NH_3 synthesis (see also Figure 2a). They assumed that the vibrational distribution function follows a Treanor distribution at T_{vib} = 3000 K, truncated at the 11th level to account for depopulation of highly excited levels. They observed a maximum TOF of 10^{-6} s^{-1} at 473 K, on the (111) metal terraces on Ru (E_b = −0.55 eV). We explicitly calculated the N_2 vibrational distribution functions in our plasma chemical kinetics models, and our models reveal a vibrational temperature up to 597 K in the filamentary regime (see Figure 2) and up to 2623 K in the uniform regime (i.e., DBD with less pronounced microdischarges, as could be relevant for packed bed DBD with packing beads of low dielectric constant).[18]

We find the same result for the effect of N_2 vibrational excitation, even with different vibrational temperatures (see Figure 2a), but we observed that the vertical and horizontal shifts of the volcano are overruled by plasma-generated radicals in both regimes (cf. Figure 4). It is possible that at lower specific energy inputs than assumed in the plasma chemistry models by van't Veer, vibrational excitations are relatively more important than plasma dissociation. In that case, the NH_3 TOF follows the volcano behavior predicted in Figure 2, rather than the horizontal trends predicted in Figure 4.

Ben Yaala et al.[16] speculated that the ER reaction $H_{(g)} + N^* \rightarrow NH^*$ dominates the NH_3 synthesis on W in low-pressure RF plasma, as opposed to the ER reaction $N_{(g)} + H^* \rightarrow NH^*$. This conclusion was made based on XPS analyses of a W catalyst pretreated with H_2 and subsequently put in contact with an N_2 plasma. Our model reveals that if both of these reactions occur, they will contribute to NH_3 production, certainly on the most noble catalysts (e.g., Ag), while on the less noble catalysts (like W) the ER reaction $N_{(g)} + H^* \rightarrow NH^*$ is predicted to be even more important (cf. Figure 6). We believe the mechanism put forward by Ben Yaala et al.[16] is too limited, because it considers plasma pretreatment with only one gas, followed by the other gas, and so it does not fully reflect the situation of NH_3 synthesis from an N_2/H_2 plasma. Indeed, our model indicates that the subsequent hydrogenations of NH* also follow an ER mechanism: $H_{(g)} + NH_x^*$. This pathway is impossible in a pure N_2 plasma, as it requires H radicals in the gas phase, and this could explain why no NH_3 was observed in their XPS analysis, when pretreating with H_2 plasma, followed by N_2 plasma.[16]

In addition, they observed higher NH_3 conversion at the 1:1 N_2/H_2 ratio in plasma catalysis, while under homogeneous plasma conditions the 1:3, stoichiometric, ratio performed better. This trend was suggested to indicate the occurrence of ER reactions under plasma-catalytic conditions. The same trend is not confirmed by the current model, which predicts that the 3:1 ratio achieves the highest TOFs (cf. Figure S11). The latter is explained by the higher density of N atoms in the 3:1 gas mixture (cf. Table S6), which was found to be the rate-limiting factor in the process (cf. Table 2). This discrepancy between model and experiments could be due to the assumption of fixed gas phase ratios in the model. The 3:1 gas mixture has higher N density, which causes higher loss rate of the N atoms, and over time the N density in the 3:1 gas ratio might become more similar to the 1:1 ratio. Our model might thus not be suited to predict reaction orders of radical species. We believe a study of reaction orders might be a valuable topic of future research, as soon as fully coupled plasma catalysis models (that simultaneously simulate surface and plasma reactions) are available to the community.

By combining experimental measurements with ab initio molecular dynamics (MD) simulations, Yamijala et al.[33] studied the performance of Fe, Pt, and Cu in low-pressure RF plasmas at a 1:3 N_2/H_2 gas composition. They concluded from the experiments, in agreement with the findings of this paper, that NH_3 yields were weakly dependent on the catalyst material. Subsequently, they used optical emission spectroscopy and MD to analyze potential mechanisms of NH_3 synthesis. Their work confirms the importance of hydrogen-terminated surfaces for the hydrogenation toward NH_3. They found that direct interaction between N and H* is possible on both Pt and Cu (the two catalysts studied via MD), but more likely to occur on Cu. Our own findings suggest that the interaction between N and H* is more likely on Pt. However, their MD simulations do not account for different H* coverages which they assumed equal on both metals. In our microkinetic simulations, the H* coverage is lower on more noble catalysts, which would lower the likelihood of the N + H* reaction. Their results also confirm the importance of hydrogenation of NH toward NH_3 via the ER mechanism with plasma-generated H, which was speculated to be the reason why the less noble catalyst performed equally well as the more noble catalysts, in agreement with our findings in section 2 (Reaction Mechanisms and Kinetics).

Hong et al.[17] suggested the following reaction pathway on Fe/Al_2O_3 catalyst in a DBD plasma, based on their plasma kinetics model with simple surface reactions:

1.	$e^- + N_2$	$\rightarrow e^- + 2N$	(plasma)
2.	$H_2 + 2^*$	$\rightarrow 2H^*$	(catalyst)
3.	$N + H$	$\rightarrow NH$	(plasma)
4.	$NH + H^*$	$\rightarrow NH_2^*$	(ER)
5a.	$NH_2 + H^*$	$\rightarrow NH_3$	(ER)
5b.	$NH_2^* + H^*$	$\rightarrow NH_3$	(LH)

In their model, they considered fixed reduced electric fields between 30 and 70 Td. The electron temperature was between 1 and 1.5 eV (compared to 6 eV during the microdischarges of our filamentary plasma and 0.7 eV during the afterglows in between the microdischarges, for our typical plasma[22]) and the vibrational temperature was approximately 700 K. On par with our results, they suggested that the NH_3 synthesis on non-noble catalysts follows a plasma-enhanced semicatalytic route, where N_2 is dissociated in the plasma and H_2 is dissociated on the surface. On the other hand, they found that NH was first created in the plasma and subsequently reacts via an ER reaction with H*. Our model suggests that NH* is created at the catalyst surface via the ER reaction N + H* during the microdischarge filaments (i.e., at maximum power density). This difference can be explained by the fact that we have a higher N density than NH density in our plasma phase. Hong et al., however, assumed a uniform plasma without microdischarges and obtained a higher NH density than the N density. They suggested that both ER and LH reactions contribute to the final hydrogenation of NH_2^*. While our model confirms that the LH reaction is relatively more important in between the microdischarges, it is still less important on the least noble catalysts.

https://doi.org/10.1021/acssuschemeng.1c02713
ACS Sustainable Chem. Eng. 2021, 9, 13151−13163

Shah et al.[34] suggested the following reaction pathway for a low-pressure RF plasma with Fe catalyst, based on a similar plasma kinetics model with simple surface reactions as developed by Hong et al.:[17]

1.	$N_2 + e^-$	$\rightarrow 2N + e^-$	(plasma)
	$H_2 + e^-$	$\rightarrow 2H + e^-$	
2.	$H + *$	$\rightarrow H*$	(catalylst)
	$N + *$	$\rightarrow N*$	
3.	$H + N*$	$\rightarrow NH*$	(EF)
4.	$NH* + H*$	$\rightarrow NH_2* + *$	(LH)
5.	$NH_2* + H*$	$\rightarrow NH_3 + 2*$	(LH)

In this pathway NH* is created via an ER mechanism, while subsequent hydrogenations follow a LH mechanism. It can be expected that in low-pressure plasmas LH reactions are relatively more important than in atmospheric pressure plasmas, because of the lower density of radicals. Shah et al.[34] indeed suggested that in DBD plasmas at atmospheric pressure ER reactions would become more important. In a different article by Shah et al.,[35] again ER reactions were found crucial for the formation of NH* and H_2 recombination, in a low-pressure RF plasma. Additionally, they suggested the existence of a "volcano" trend when plotting the TOF against a linear combination of the activation barriers of H_2 recombination, H-bulk diffusion and NH* formation. Direct comparison to their volcano must be done carefully, as their independent variable does not arrange the transition metals in the same way as in this paper or in the models by Mehta et al.[4] and Vojvodic et al.[3]

Wang et al.[32] showed a correlation between the concentration of strong acid sites of Al_2O_3 supported Fe, Ni, and Cu and the NH_3 yields and TOFs. In agreement with Mehta et al.,[4] they concluded that in plasma catalysis the more noble catalysts Ni and Cu perform better than Fe, which is generally used for thermal catalytic NH_3 synthesis. However, while Mehta et al. predicted a steep decrease in NH_3 TOF (more than a factor 10^{10}, as also indicated by Figure 2), the performance of Ni and Cu was almost identical in the experiments of Wang et al.[32] This is indeed also what our model predicts for a filamentary discharge, as well as for a uniform discharge, like studied by Wang et al. (cf. Figure 4). The lower performance of Fe compared to Ni and Cu could indicate that our model underestimates the barriers of ER reactions on the least-noble catalysts. The observed trend might be more on par with the calculated TOF when assuming ER barriers of, e.g., 0.3 eV, as shown in Figure 5c and discussed in the section Sensitivity Analysis of the Eley−Rideal Reactions.

Another explanation for the lower performance of Fe was given by Winter et al.[36] By means of FTIR spectroscopy, they observed the formation of N_2H_y species on the Fe catalyst, impeding the production of NH_3. While the reactions of N_2H_y species are not included in our model, these species can only be formed as the coverage of NH_x species increases. In Figure S11 of the Supporting Information, we show that during the afterglows of the filamentary plasma, catalysts with a binding energy stronger or equal to Fe become entirely covered with NH. Under these conditions it is likely that N_2H_y species are being formed, lowering the NH_3 TOF on catalysts that bind NH_x species more strongly or as strongly as Fe.

Patil et al.[11] studied the influence of the feed ratio (N_2/H_2), specific energy input, reaction temperature, metal loading, and gas flow rates on the yield and energy efficiency of NH_3 production. One of their conclusions was that Al_2O_3 loaded with 10 wt % Fe and Mn provided lower NH_3 concentrations than Al_2O_3 loaded with 10 wt % Ni, Co, or Mo. In other words, in their setup, NH_3 production is dependent on the catalyst material. However, they attributed this change in reactivity to the physical influence of the catalyst on the discharge mode. Fe/Al_2O_3 and Mn/Al_2O_3 showcased significantly less discharges and were operating more in a nonfilamentary regime, in contrast with the other catalysts. These results can thus not be compared to the modeling results in the previous sections, where the same plasma conditions were assumed for each of the catalyst materials in order to study the chemical properties of the metal, instead of the physical properties.

CONCLUSION

In the case of plasma-enhanced catalytic NH_3 synthesis, i.e., when only vibrational excitations are important, our model results predict that optimal catalyst materials are strongly dependent on the imposed VDFs. Specifically, more noble catalysts (metals such as Rh, Ni, Pt, and Pd) are found to optimize TOFs depending on the population of the higher energy levels. The population of higher energy levels is found to be more important than the vibrational temperature.

In the case where radicals are present in the plasma phase (with concentrations calculated via plasma chemistry models), the process follows a surface-enhanced plasma-driven synthesis; i.e., radicals are the primary source of N and H. Under these conditions, radical adsorption reactions are found to largely remove the dependency of TOFs on the catalyst binding energy of the more noble catalysts. Additionally, Eley−Rideal reactions are found to largely remove the dependency of TOFs on the catalyst binding energy on the less noble catalysts. In this way, the reactions of plasma-generated radicals counter the volcano behavior from thermal conditions and from plasma conditions that only include vibrational excitation.

Under the conditions studied in this paper, the plasma/catalyst system appears to be closer to the latter regime than the former, acknowledging direct comparisons are difficult. For all calculated radical densities and VDFs, including uniform and filamentary DBD plasmas, and both inside and in between the microdischarges, the reactions of plasma-generated radicals have more impact on the NH_3 TOF than the catalytic dissociation of vibrationally excited N_2 molecules. The NH_3 TOF in the afterglows of the microdischarges were found to be a factor 10^{10} higher than the thermal TOF, and the TOFs inside the microdischarges and in the uniform plasma were found to be another factor 10^3 and 10^4 higher than in the afterglows. In each case, the TOFs are between 10^6 and 10^{10} times higher than when only vibrational excitations are assumed in the absence of radicals.

Under the conditions of high radical densities, we showed that on all catalysts, NH_3 TOFs are directly related to the density of N atoms. Because radical adsorptions and ER reactions are assumed barrierless and because the coverage of H* on non-noble catalysts and the coverage of free sites on noble catalysts are close to unity, our model reveals that the TOFs are independent of the catalyst material in the entire range of catalysts studied.

We conclude that the models presented in this article elucidate trends and concepts reported in previous research, despite the different plasma conditions studied in each of these works. Moreover, the detailed comparison between the different contributions of plasma species and their reactions show the individual impact of each of these effects on the NH_3 production, complementing the current state of knowledge, which is much needed for further advancement in the field.

https://doi.org/10.1021/acssuschemeng.1c02713
ACS Sustainable Chem. Eng. 2021, 9, 13151−13163

■ ASSOCIATED CONTENT

Supporting Information

The Supporting Information is available free of charge at https://pubs.acs.org/doi/10.1021/acssuschemeng.1c02713.

Kinetic data, gas phase densities, DFT calculations, sensitivity analyses, reaction rates, reaction pathways in the afterglows, TOF results at higher temperature, ratio of contribution of ER to LH reactions, coverage of species in the afterglows of the filamentary plasma, simulation of different gas ratios, (PDF)

■ AUTHOR INFORMATION

Corresponding Author

Yannick Engelmann − *Department of Chemistry, Research Group PLASMANT, PLASMA and NANOLab Centers of Excellence, Universiteit Antwerpen, 2610 Wilrijk-Antwerp, Belgium;* orcid.org/0000-0002-0894-8192; Email: yannick.engelmann@uantwerpen.be

Authors

Kevin van 't Veer − *Department of Chemistry, Research Group PLASMANT, PLASMA and NANOLab Centers of Excellence, Universiteit Antwerpen, 2610 Wilrijk-Antwerp, Belgium; Faculty of Sciences, Chemistry of Surfaces, Interfaces and Nanomaterials, CP255, Université Libre de Bruxelles, B-1050 Brussels, Belgium;* orcid.org/0000-0003-2540-467X

Yury Gorbanev − *Department of Chemistry, Research Group PLASMANT, PLASMA and NANOLab Centers of Excellence, Universiteit Antwerpen, 2610 Wilrijk-Antwerp, Belgium;* orcid.org/0000-0002-8059-4464

Erik Cornelis Neyts − *Department of Chemistry, Research Group PLASMANT, PLASMA and NANOLab Centers of Excellence, Universiteit Antwerpen, 2610 Wilrijk-Antwerp, Belgium;* orcid.org/0000-0002-3360-3196

William F. Schneider − *Department of Chemical and Biomolecular Engineering, University of Notre Dame, Notre Dame, Indiana 46556, United States;* orcid.org/0000-0003-0664-2138

Annemie Bogaerts − *Department of Chemistry, Research Group PLASMANT, PLASMA and NANOLab Centers of Excellence, Universiteit Antwerpen, 2610 Wilrijk-Antwerp, Belgium;* orcid.org/0000-0001-9875-6460

Complete contact information is available at: https://pubs.acs.org/10.1021/acssuschemeng.1c02713

Notes

The authors declare no competing financial interest.

■ ACKNOWLEDGMENTS

We acknowledge the financial support from the DOC-PRO3, the TOP-BOF, and the Methusalem project of the University of Antwerp, as well as from the European Research Council (ERC) (grant agreement No, 810182−SCOPE ERC Synergy project), under the European Union's Horizon 2020 research and innovation programme, the Flemish Government through the Moonshot cSBO project P2C (HBC.2019.0108), and the Excellence of Science FWO-FNRS project (FWO grant ID GoF9618n, EOS ID 30505023). Calculations were carried out using the Turing HPC infrastructure at the CalcUA core facility of the Universiteit Antwerpen, a division of the Flemish Supercomputer Center VSC, funded by the Hercules Foundation, the Flemish Government (Department EWI), and the University of Antwerp. Support for W.F.S. was provided by the U.S. Department of Energy, Office of Science, Office of Basic Energy Sciences, under Award DE-SC0021107."

■ REFERENCES

(1) Patil, B. S.; Wang, Q.; Hessel, V.; Lang, J. Plasma N2 -Fixation: 1900 - 2014. *Catal. Today* **2015**, *256*, 49−66.

(2) Guo, J.; Chen, P. Catalyst: NH3 as an Energy Carrier. *Chem.* **2017**, *3* (5), 709−712.

(3) Vojvodic, A.; Medford, A. J.; Studt, F.; Abild-Pedersen, F.; Khan, T. S.; Bligaard, T.; Nørskov, J. K. Exploring the Limits: A Low-Pressure, Low-Temperature Haber-Bosch Process. *Chem. Phys. Lett.* **2014**, *598*, 108−112.

(4) Mehta, P.; Barboun, P.; Herrera, F. A.; Kim, J.; Rumbach, P.; Go, D. B.; Hicks, J. C.; Schneider, W. F. Overcoming Ammonia Synthesis Scaling Relations with Plasma-Enabled Catalysis. *Nat. Catal.* **2018**, *1* (4), 269−275.

(5) Mehta, P.; Barboun, P.; Go, D. B.; Hicks, J. C.; Schneider, W. F. Catalysis Enabled by Plasma Activation of Strong Chemical Bonds: A Review. *ACS Energy Lett.* **2019**, *4* (5), 1115−1133.

(6) Mehta, P.; Barboun, P. M.; Engelmann, Y.; Go, D. B.; Bogaerts, A.; Schneider, W. F.; Hicks, J. C. Plasma-Catalytic Ammonia Synthesis Beyond the Equilibrium Limit. *ACS Catal.* **2020**, *10* (12), 6726−6734.

(7) Mizushima, T.; Matsumoto, K.; Ohkita, H.; Kakuta, N. Catalytic Effects of Metal-Loaded Membrane-like Alumina Tubes on Ammonia Synthesis in Atmospheric Pressure Plasma by Dielectric Barrier Discharge. *Plasma Chem. Plasma Process.* **2007**, *27* (1), 1−11.

(8) Barboun, P.; Mehta, P.; Herrera, F. A.; Go, D. B.; Schneider, W. F.; Hicks, J. C. Distinguishing Plasma Contributions to Catalyst Performance in Plasma-Assisted Ammonia Synthesis. *ACS Sustainable Chem. Eng.* **2019**, *7* (9), 8621−8630.

(9) Herrera, F. A.; Brown, G. H.; Barboun, P.; Turan, N.; Mehta, P.; Schneider, W. F.; Hicks, J. C.; Go, D. B. The Impact of Transition Metal Catalysts on Macroscopic Dielectric Barrier Discharge (DBD) Characteristics in an Ammonia Synthesis Plasma Catalysis Reactor. *J. Phys. D: Appl. Phys.* **2019**, *52* (22), 224002.

(10) Iwamoto, M.; Akiyama, M.; Aihara, K.; Deguchi, T. Ammonia Synthesis on Wool-like Au, Pt, Pd, Ag, or Cu Electrode Catalysts in Nonthermal Atmospheric-Pressure Plasma of N2 and H2. *ACS Catal.* **2017**, *7* (10), 6924−6929.

(11) Patil, B. S.; Cherkasov, N.; Srinath, N. V.; Lang, J.; Ibhadon, A. O.; Wang, Q.; Hessel, V. The Role of Heterogeneous Catalysts in the Plasma-Catalytic Ammonia Synthesis. *Catal. Today* **2021**, *362*, 2−10.

(12) Iwamoto, M.; Horikoshi, M.; Hashimoto, R.; Shimano, K.; Sawaguchi, T.; Teduka, H.; Matsukata, M. Higher Activity of Ni/γ-Al2O3 over Fe/γ-Al2O3 and Ru/γ- Al2O3 for Catalytic Ammonia Synthesis in Nonthermal Atmospheric-Pressure Plasma of N2 and H2. *Catalysts* **2020**, *10* (5), 590.

(13) Akiyama, M.; Aihara, K.; Sawaguchi, T.; Matsukata, M.; Iwamoto, M. Ammonia Decomposition to Clean Hydrogen Using Non-Thermal Atmospheric-Pressure Plasma. *Int. J. Hydrogen Energy* **2018**, *43* (31), 14493−14497.

(14) Rouwenhorst, K. H. R.; Kim, H.-H.; Lefferts, L. Vibrationally Excited Activation of N2 in Plasma-Enhanced Catalytic Ammonia Synthesis: A Kinetic Analysis. *ACS Sustainable Chem. Eng.* **2019**, *7* (20), 17515−17522.

(15) Wang, L.; Zhao, Y.; Liu, C.; Gong, W.; Guo, H. Plasma Driven Ammonia Decomposition on a Fe-Catalyst: Eliminating Surface Nitrogen Poisoning. *Chem. Commun.* **2013**, *49* (36), 3787−3789.

(16) Ben Yaala, M.; Saeedi, A.; Scherrer, D. F.; Moser, L.; Steiner, R.; Zutter, M.; Oberkofler, M.; De Temmerman, G.; Marot, L.; Meyer, E. Plasma-Assisted Catalytic Formation of Ammonia in N2-H2 Plasma on a Tungsten Surface. *Phys. Chem. Chem. Phys.* **2019**, *21* (30), 16623−16633.

(17) Hong, J.; Pancheshnyi, S.; Tam, E. Kinetic Modelling of NH3 Production in N2-H2 Non-Equilibrium Atmospheric-Pressure Plasma Catalysis Related Content. *J. Phys. D: Appl. Phys.* **2017**, *50*, 154005.

(18) Wang, W.; Kim, H.; Laer, K.; Van Bogaerts, A. Streamer Propagation in a Packed Bed Plasma Reactor for Plasma Catalysis Applications. *Chem. Eng. J.* **2018**, *334* (September 2017), 2467−2479.
(19) Shah, J. R.; Gorky, F.; Lucero, J.; Carreon, M. A.; Carreon, M. L. Ammonia Synthesis via Atmospheric Plasma Catalysis: Zeolite 5A, a Case of Study. *Ind. Eng. Chem. Res.* **2020**, *59* (11), 5167−5176.
(20) Shah, J.; Wu, T.; Lucero, J.; Carreon, M. A.; Carreon, M. L. Nonthermal Plasma Synthesis of Ammonia over Ni-MOF-74. *ACS Sustainable Chem. Eng.* **2019**, *7* (1), 377−383.
(21) Gorky, F.; Guthrie, S. R.; Smoljan, C. S.; Crawford, J. M.; Carreon, M. A.; Carreon, M. L. Plasma Ammonia Synthesis over Mesoporous Silica SBA-15. *J. Phys. D: Appl. Phys.* **2021**, *54* (26), 264003.
(22) van 't Veer, K.; Engelmann, Y.; Reniers, F.; Bogaerts, A. Plasma-Catalytic Ammonia Synthesis in a DBD Plasma: Role of Micro-discharges and Their Afterglows. *J. Phys. Chem. C* **2020**, *124* (42), 22871−22883.
(23) Ma, H.; Schneider, W. F. Structure- and Temperature-Dependence of Pt-Catalyzed Ammonia Oxidation Rates and Selectivities. *ACS Catal.* **2019**, *9* (3), 2407−2414.
(24) Engelmann, Y.; Mehta, P.; Neyts, E. C.; Schneider, W. F.; Bogaerts, A. Predicted Influence of Plasma Activation on Nonoxidative Coupling of Methane on Transition Metal Catalysts. *ACS Sustainable Chem. Eng.* **2020**, *8* (15), 6043−6054.
(25) Hummelshøj, J. S.; Abild-Pedersen, F.; Studt, F.; Bligaard, T.; Nørskov, J. K. CatApp: A Web Application for Surface Chemistry and Heterogeneous Catalysis. *Angew. Chem., Int. Ed.* **2012**, *51* (1), 272−274.
(26) Nørskov Jens, K., Felix, Studt, Frank Abild-Pedersen, T. B. *Fundamental Concepts in Heterogeneous Catalysis*, First ed.; John Wiley & Sons, 2014.
(27) Fuller, J.; Fortunelli, A.; Goddard, W. A.; An, Q. Reaction Mechanism and Kinetics for Ammonia Synthesis on the Fe(211) Reconstructed Surface. *Phys. Chem. Chem. Phys.* **2019**, *21* (21), 11444−11454.
(28) van 't Veer, K.; Reniers, F.; Bogaerts, A. Zero-Dimensional Modelling of Unpacked and Packed Bed Dielectric Barrier Discharges: The Role of Vibrational Kinetics in Ammonia Synthesis. *Plasma Sources Sci. Technol.* **2020**, *29* (4), 045020.
(29) Pancheshnyi, S.; Eismann, B.; Hagelaar, G. J. M.; Pitchford, L. C. *Computer code ZDPlasKin*, http://www.zdplaskin.laplace.univ-tlse.fr; University of Toulouse, LAPLACE, CNRS-UPS-INP, Toulouse, France, 2008.
(30) Hagelaar, G. J. M.; Pitchford, L. C. Solving the Boltzmann Equation to Obtain Electron Transport Coefficients and Rate Coefficients for Fluid Models. *Plasma Sources Sci. Technol.* **2005**, *14* (4), 722−733.
(31) Fridman, A. *Plasma Chemistry*; Cambridge University Press, 2008. DOI: 10.1017/CBO9780511546075.
(32) Wang, Y.; Craven, M.; Yu, X.; Ding, J.; Bryant, P.; Huang, J.; Tu, X. Plasma-Enhanced Catalytic Synthesis of Ammonia over a Ni/Al2O3 Catalyst at Near-Room Temperature: Insights into the Importance of the Catalyst Surface on the Reaction Mechanism. *ACS Catal.* **2019**, *9*, 10780−10793.
(33) Yamijala, S. S. R. K. C.; Nava, G.; Ali, Z. A.; Beretta, D.; Wong, B. M.; Mangolini, L. Harnessing Plasma Environments for Ammonia Catalysis: Mechanistic Insights from Experiments and Large-Scale Ab Initio Molecular Dynamics. *J. Phys. Chem. Lett.* **2020**, *11* (24), 10469−10475.
(34) Shah, J.; Wang, W.; Bogaerts, A.; Carreon, M. L. Ammonia Synthesis by Radio Frequency Plasma Catalysis: Revealing the Underlying Mechanisms. *ACS Appl. Energy Mater.* **2018**, *1* (9), 4824−4839.
(35) Shah, J.; Gorky, F.; Psarras, P.; Seong, B.; Gómez-Gualdrón, D. A.; Carreon, M. L. Enhancement of the Yield of Ammonia by Hydrogen-Sink Effect during Plasma Catalysis. *ChemCatChem* **2020**, *12*, 1200.
(36) Winter, L. R.; Ashford, B.; Hong, J.; Murphy, A. B.; Chen, J. G. Identifying Surface Reaction Intermediates in Plasma Catalytic Ammonia Synthesis. *ACS Catal.* **2020**, *10* (24), 14763−14774.